NANO LETTERS

Letter

pubs.acs.org/NanoLett

# Oxygen Release Induced Chemomechanical Breakdown of Layered Cathode Materials

Linqin Mu,[†] Ruoqian Lin,[‡] Rong Xu,[§] Lili Han,[∥] Sihao Xia,[⊥] Dimosthenis Sokaras,[⊥] James D. Steiner,[†] Tsu-Chien Weng,[#] Dennis Nordlund,[⊥] Marca M. Doeff,[▽] Yijin Liu,[⊥] Kejie Zhao,[§] Huolin L. Xin,*[,‡] and Feng Lin*[,†]

[†]Department of Chemistry, Virginia Tech, Blacksburg, Virginia 24061, United States

[‡]Center for Functional Nanomaterials, Brookhaven National Laboratory, Upton, New York 11973, United States

[§]School of Mechanical Engineering, Purdue University, West Lafayette, Indiana 47907, United States

[∥]Center for Electron Microscopy, TUT-FEI Joint Laboratory, Institute for New Energy Materials & Low-Carbon Technologies, School of Materials Science and Engineering, Tianjin University of Technology, Tianjin 300384, China

[⊥]Stanford Synchrotron Radiation Lightsource, SLAC National Accelerator Laboratory, Menlo Park, California 94025, United States

[#]Center for High Pressure Science & Technology Advanced Research, Shanghai 201203, China

[▽]Energy Storage and Distributed Resources Division, Lawrence Berkeley National Laboratory, Berkeley, California 94720, United States

Supporting Information

**ABSTRACT:** Chemical and mechanical properties interplay on the nanometric scale and collectively govern the functionalities of battery materials. Understanding the relationship between the two can inform the design of battery materials with optimal chemomechanical properties for long-life lithium batteries. Herein, we report a mechanism of nanoscale mechanical breakdown in layered oxide cathode materials, originating from oxygen release at high states of charge under thermal abuse conditions. We observe that the mechanical breakdown of charged $Li_{1-x}Ni_{0.4}Mn_{0.4}Co_{0.2}O_2$ materials proceeds via a two-step pathway involving intergranular and intragranular crack formation. Owing to the oxygen release, sporadic phase transformations from the layered structure to the spinel and/or rocksalt structures introduce local stress, which initiates microcracks along grain boundaries and ultimately leads to the detachment of primary particles, *i.e.*, intergranular crack formation. Furthermore, intragranular cracks (pores and exfoliations) form, likely due to the accumulation of oxygen vacancies and continuous phase transformations at the surfaces of primary particles. Finally, finite element modeling confirms our experimental observation that the crack formation is attributable to the formation of oxygen vacancies, oxygen release, and phase transformations. This study is designed to directly observe the chemomechanical behavior of layered oxide cathode materials and provides a chemical basis for strengthening primary and secondary particles by stabilizing the oxygen anions in the lattice.

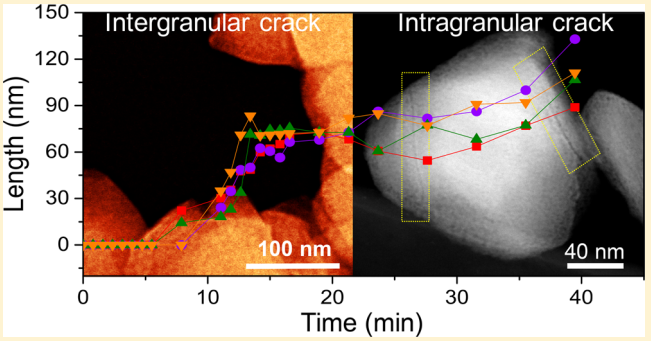


**KEYWORDS:** *Cathode, crack, phase transformation, oxygen release*

Since the inauguration of implementing $LiCoO_2$ materials in commercial lithium ion batteries, a number of cathode materials derived from $LiCoO_2$ have been investigated and applied in practical batteries. In particular, $LiNi_{1-x-y}Mn_xCo_yO_2$ (NMC) materials, with Ni and Mn cosubstituting the Co site in $LiCoO_2$, are regarded as the most promising $LiCoO_2$ derivatives that can potentially improve practical energy density, reduce cost, and enhance safety characteristics of batteries for fast-growing applications, such as electric vehicles and grid energy storage.[1−3] However, challenges at the length scales of active particles,[4,5] electrodes,[6−9] and interfaces in full cells[10−12] have decelerated the pace of their substitution for the expensive $LiCoO_2$ in the market. Stoichiometric NMC materials usually consist of nanometric primary particles assembled into 3D hierarchical structures (larger secondary particles).[13−16] Performance degradation of cathodes containing NMC materials may be attributed to formation of microcracks between primary particles,[17] electrolyte decomposition,[18,19] undesired phase transformations such as surface reconstruction,[4,5] and dissolution of transition metal cations.[20]

Received: March 14, 2018
Revised: April 11, 2018
Published: April 18, 2018





DOI: 10.1021/acs.nanolett.8b01036
Nano Lett. XXXX, XXX, XXX−XXX

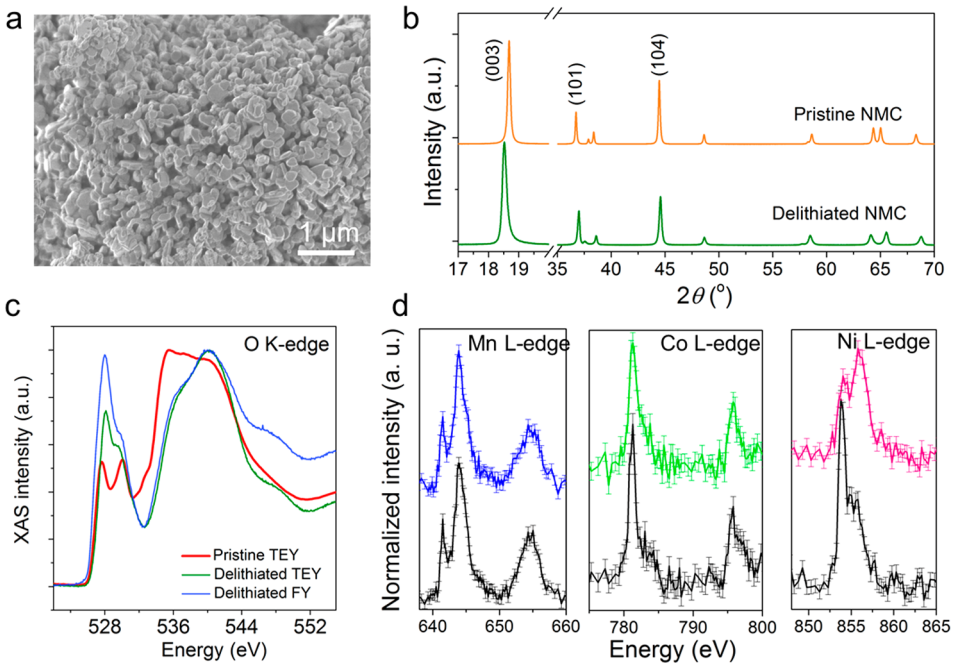


**Figure 1.** (a) SEM image of the pristine NMC material. (b) XRD patterns of pristine and delithiated NMC materials. (c) O K-edge XAS collected in the TEY and FY modes for pristine (red/TEY) and delithiated (green/TEY and blue/FY) NMC materials. (d) TM L-edge XRS of pristine (bottom) and delithiated (top) NMC materials. The error bars were calculated based on the standard deviations of six repeated data acquisitions under identical experimental conditions.

These processes are highly correlated at the atomic scale. Because of the hybridization between transition metal (TM) 3d and O 2p orbitals and local coordination chemistry in oxide cathode materials (including NMCs), d holes generated during lithium deintercalation partially reside on O 2p orbitals, which activates oxygen anions,[21−23] accelerates electrolyte oxidation, and results in reduced transition metal oxides on particle surfaces, *e.g.*, rocksalt formation.[4,24,25] The volume change upon charging/discharging causes local stresses that can induce microcracks in 3D hierarchical NMC structures.[26,27] Microcracks increase the exposed surface area to electrolytic solution leading to more severe electrolyte oxidation and rocksalt formation, especially at high operating voltages.[28] The aforementioned challenges prevail in almost all oxide-based cathode materials.[4,25,26,28,29]

Crack formation has been reported in many studies as one of the important failure mechanisms in battery cathodes.[27,30−32] Their formation is generally categorized as either intragranular or intergranular, where the former occurs within the primary particles, and the latter occurs along grain boundaries, *i.e.*, in between primary particles. Yan et al. reported intragranular crack formation in a commercial $LiNi_{1/3}Mn_{1/3}Co_{1/3}O_2$ material when charged up to 4.7 V in lithium half cells, which are closely related to dislocations.[26] Intragranular cracks were also observed in Li-rich and Mn-rich cathode materials, resulting in voltage decay and capacity fade.[29,33] Crack formation can be attributed to the periodic lattice expansion and contraction upon long-term cycling, similar to the fatigue phenomenon in materials under cyclic loading. Oxygen activity and gas release phenomena are frequently observed in lithium-rich layered oxide cathode materials.[21,23] For stoichiometric NMC materials, however, it is somewhat unclear and debatable how much oxygen activity functions in the charge compensation.[34,35] Nevertheless, it is the general consensus that depleting O 2p orbitals can result in the oxidation of electrolyte and reduction of transition metals at the surface of NMC particles.[4,24,36] Furthermore, depleting O 2p orbitals increases the risk of oxygen gas release under thermal abuse conditions, especially at high states of charge.[37] Apart from safety concerns,[31] the phase transformation that arises from oxygen release creates local stresses that can potentially lead to the chemomechanical breakdown, namely, formation of microcracks.[38]

Herein, by virtue of *in situ* environmental transmission electron microscopy (ETEM), we studied the morphology transformation of charged NMC particle ensembles under thermal abuse conditions. Two distinct processes took place at the nanometric scale. First, the particle ensembles underwent intergranular crack formation at the boundaries after a short incubation period. Second, the nanopores propagated in primary NMC particles, grew to larger pores/exfoliations (intragranular cracks), and eventually led to the mechanical breakdown of primary particles. Throughout the entire process, we observed continuous reduction of transition metals, formation of spinel/rocksalt phases, as well as oxygen release. The oxygen release accelerates the mechanical breakdown of delithiated NMC materials. Meanwhile, finite element modeling was performed to provide insights into the formation and propagation of the oxygen release and subsequent chemomechanical breakdown of NMC cathode materials. Finally, complementary to the *in situ* heating with TEM visualization, we observed extensive crack formation in secondary particles using transmission X-ray tomography for particles after long-term cycles. Our study highlights the importance of controlling local stresses in 3D NMC hierarchical structures at high states of charge under thermal abuse conditions.

**Characterization.** Battery materials inevitably operate outside the electrochemical stability window of the electrolytic solution, which is defined by the highest occupied molecular orbital (HOMO) and the lowest unoccupied molecular orbital (LUMO) of its constituents. Electrode−electrolyte interactions


DOI: 10.1021/acs.nanolett.8b01036
*Nano Lett.* XXXX, XXX, XXX−XXX

complicate the surface chemistry of cathode materials, which inevitably undermines the determination of intrinsic electrochemical properties. Chemical delithiation, in contrast, provides an efficient path toward preparing charged materials without the interference of electrode−electrolyte side reactions. In this study, we first synthesized $LiNi_{0.4}Mn_{0.4}Co_{0.2}O_2$ (NMC) powder using a coprecipitation method (see the Experimental Section). The primary particles (100−300 nm) are agglomerated into a porous architecture (Figure 1a) that allows for the rapid percolation of oxidative solution during the subsequent chemical delithiation. The synthesis results in NMC particles with a broad distribution of morphologies. Importantly, we could identify secondary particles that consisted of only a few primary particles rather than big agglomerations under TEM (shown later). These secondary particles are good candidates for *in situ* TEM study given the limited penetration depth of electron beams. The previously described chemical delithiation method[39,40] resulted in a lithium-poor NMC powder (delithiated NMC), which retained the $\alpha$-$NaFeO_2$ layered structure with the space group of $R\bar{3}m$. The (003) peak of delithiated NMC shifted to a lower angle, indicating that the stronger layer−layer repulsion results in expansion of the *c*-axis space (Figure 1b). Due to the strong oxidation reaction, we occasionally found exfoliation in the primary particles (Figure S1).[41] We then characterized the electronic structures of the transition metal (TM) cations before and after chemical delithiation via soft X-ray absorption spectroscopy (XAS) and X-ray Raman spectroscopy (XRS). The TM 3d−O 2p hybridization in the $TMO_6$ octahedral cluster gives rise to distinctive pre-edge peaks between 525 and 533 eV in the O K-edge XAS spectra (Figure 1c). The nature of the hybridization, such as delocalization of hole states, is rather complicated and under debate.[42] Nevertheless, it is generally accepted that the intensity of the pre-edge peak is in a positive relationship with the total hole concentration in the $TMO_6$ cluster.[34,43,44] The intensity of the pre-edge peak increases after chemical delithiation (Figure 1c), and exhibits a depth-dependent behavior;[26,43,45] namely, the bulk (probed by fluorescence yield, FY, 50−100 nm) shows a higher hole concentration than the surface (probed by total electron yield, TEY, 5−10 nm). This observation is consistent with recent studies showing that oxygen activity, *i.e.*, O 2p occupancy, shows depth-dependent behaviors.[24,35,43,45] X-ray Raman spectroscopy (XRS) is a powerful technique to measure TM L-edge spectra with bulk sensitivity. Overall, Ni experienced a dramatic increase of valence state, while Mn and Co remained unchanged after chemical delithiation (Figure 1d).[34,44] It should be noted that Co redox in NMC materials is still debatable. We did not observe Co also likely due to the limited energy resolution of XRS. Nevertheless, our study demonstrates that we have successfully chemically delithiated NMC and that the charge compensation is via depletion of electrons in O 2p and Ni 3d orbitals (oxygen is activated). Based on the reported Ni L-edge and O K-edge XAS and XRS at the given states of charge, we estimated that the chemically delithiated NMC powder had approximately 60% of the lithium removed.[24] The chemical composition was then measured by the inductively couple plasma−optical emission spectrometry (ICP−OES) to be $Li_{0.5}Ni_{0.4}Mn_{0.4}Co_{0.2}O_2$. The chemically delithiated sample was equivalent to the NMC material electrochemically charged to 4.3 V.[4,46] Hereafter, we refer to the sample as delithiated NMC. We chose chemically delithiated samples over the electrochemically delithiated counterparts because the former could provide less reduced surfaces thus more oxygen release upon *in situ* heating to amplify the observation. Such a choice does not undermine our conclusion in this work because both samples would release oxygen upon heating.

According to our recent study,[41] chemical delithiation can represent electrochemical delithiation in terms of the bulk electronic structures (oxygen activation, oxidation of transition metals). There was disintegration of secondary particles after chemical delithiation. To observe the crack formation under *in situ* TEM heating condition, disintegrated secondary particles (with a few particles connected with each other) are good because otherwise it is hard for the electron beam to penetrate thick secondary particles. We then performed *in situ* heating experiments on the delithiated NMC particles, using an ETEM, to directly visualize the chemomechanical breakdown. Under normal battery cycling conditions, the oxygen loss occurred through the interfacial reaction between the lattice oxygen and the electrolyte after NMC particles are electrochemically delithiated. In this present study, we chose to perform *in situ* TEM at 230 °C to exponentially accelerate the oxygen release and phase transformation so that we could observe chemomechanical breakdown of NMC particles within a reasonable time frame for the *in situ* TEM observation. *Z*-contrast scanning transmission electron microscopy (STEM) movies were continuously recorded during the entire heating process (a representative accelerated STEM movie is provided in the Supporting Information, Movie S1). Our previous study showed that the chemical delithiation process could introduce microcracks (Figure S1);[41] thus in this study we specifically identified particle ensembles that had no microcracks prior to *in situ* heating in TEM. We tracked the nucleation and propagation of microcracks along grain boundaries during this early stage of chemomechanical breakdown (Movie S1). Figure 2a−d shows four representative STEM images that reveal the characteristic evolution of microcracks. Upon heating at 230 °C, several slender microcracks were generated in sporadic spots and grew quickly in length and breadth after a short incubation period (~7 min), reaching ~70 nm at 15 min. Then, the speed of propagation decelerated and stayed mostly unchanged for another 15 min. Finally, the length reached about 90 nm after 40 min. During this stage, the chemomechanical breakdown took place along grain boundaries (intergranular regions), likely due to the plethora of defects and lattice mismatch near grain boundaries. Grain boundaries are 2-dimensional (2D) defects, usually the weakest regions in cathode secondary particles, and are reported to disintegrate after long-term battery cycling.[17,26] Notably, the above quantification method, based on 2D STEM images, does not fully account for the propagation of microcracks in the bulk region of the particles, which were further investigated by three-dimensional (3D) STEM tomography (discussed later in the work). Our subsequent spectroscopic and finite element analyses in this work showed that the oxygen release induced phase transformation is the main driving force responsible for the crack formation (see next).

In addition to the formation of intergranular cracks, pores and layer exfoliation (intragranular cracks) were generated in individual primary particles upon extended heating (10 h). Figure S4 shows the TEM images of these individual particles. The relatively dark and light colors are related to the thick and thin regions of particles (mass−thickness contrast, Figure S4a). To enhance the visualization, we colored the thick regions with blue and thin regions with yellow, where many nanopores of


DOI: 10.1021/acs.nanolett.8b01036
Nano Lett. XXXX, XXX, XXX−XXX

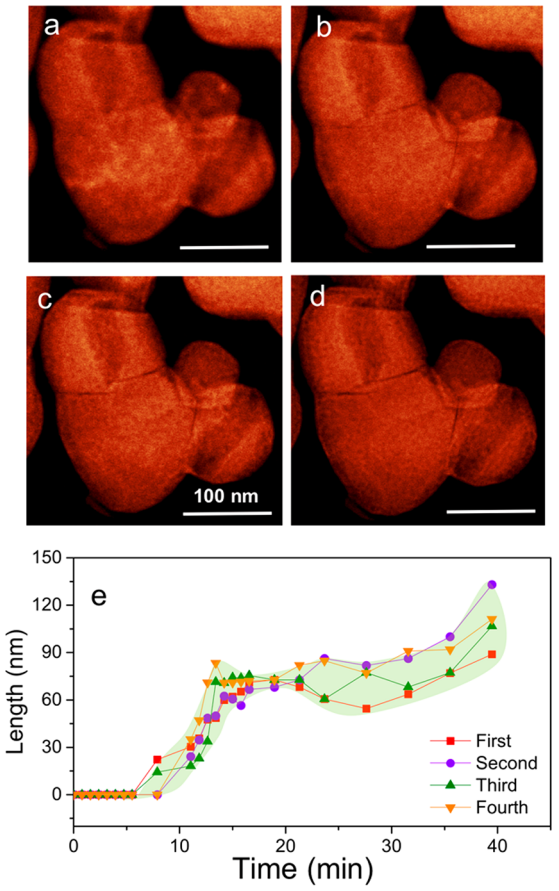


**Figure 2.** Selected *Z*-contrast scanning transmission electron microscopy (STEM) images to represent the evolution of a typical intergranular crack upon thermal activation: (a) 0, (b) 12, (c) 26, and (d) 40 min. (e) Evolution of crack length as a function of time, where four cracks (indicated by arrows in Figure S2) were independently measured and are presented here.

approximately 10 nm can be directly visualized (Figure S4b). Some of the pores link together to form a pore-cluster catkin-like morphology around the individual particles. Additionally, some particles show exfoliations (one kind of intragranular crack) (Figure S4c). Pores (surfaces) and exfoliations (most likely between (003) plane) occur inside the individual particles where the interaction between atomic layers is weak, which is a possible pathway for intragranular cracks.[26] Furthermore, the wrinkles pointed by arrows in Figure S4d are most likely associated with the one-dimensional local strain. Previous studies uncovered that oxygen release could lead to phase transformations of cathode particles.[45,46] Fast Fourier transform (FFT) and inverse fast Fourier transform (IFFT) were performed to illustrate the details of phase transformation after *in situ* heating (Figure S4e,f). Regions with layered structures are isolated from the continuous spinel/rocksalt matrix (Figure S4f). The phase boundaries are random and closely accompanied by the propagation of transition metal redox transformations.[47]

Electron energy loss spectroscopy (EELS) was performed on delithiated NMC and *in situ* heated NMC to further understand the underlying processes of forming microcracks. Several recent studies showed that electrochemically delithiated cathode particles displayed a gradient in the distribution of TM valence states due to the electrode−electrolyte side reactions and surface reconstruction.[4,47,48] Similar to the gradient distribution of hole states on the oxygen site (Figure 1c), we also observed the gradient distribution of Ni oxidation states in the delithiated particles (lower oxidation state in the surface), as shown in Figure S3. Furthermore, consistent with the O K-edge soft XAS results (Figure 1c), the O K-edge EELS underwent a red-shift in the pre-edge (TM 3d−O 2p) (Figure 3b), and the intensity of the pre-edge peak gradually increased in the first 5 nm and then leveled off (Figure 3b,c). The spatially resolved TM L-edge EELS spectra, particularly the Mn L-edge, marginally shifted to higher energy from the top surface to the subsurface, which indicates that the chemical delithiation has a similar effect on the gradient distribution of TM valence state. Since there was no electrolyte exposure in these chemically delithiated particles, we conjecture that the surface TM reduction was attributable to oxygen release when handling the sample in the glovebox. For the delithiated NMC particle after heating, EELS of three selected square (10 nm by 10 nm) regions with and without pores were collected for a comparison. We observed that the energy for the TM L-edges at the subsurface (*i.e.*, 20 nm in for pores present in the green and red rectangles) is lower than that of bulk (pore-free area in the blue rectangle) (Figure 3d,e). Therefore, the reduced layer (10−50 nm) on the heated particle is much thicker than that on the pristine (5 nm), delithiated particle, suggesting that the heating further reduces the transition metal and propagates the spinel/rocksalt layer. The pre-edge peak of the O K-edge EELS was expected to decrease due to the hybridization between TM 3d and O 2p orbitals and local coordination chemistry in oxide cathode materials.[24,25,29,49,50] In addition, we weighed the mass of delithiated NMC powder before and after heat treatment in the tube furnace at 230 °C for 3 h. The primary mass of the delithiated NMC powder decreased by approximately 3 ± 1.5% (mass ratio) due to the oxygen loss during the heat treatment, assuming that other elements are not volatile at such a low temperature. The oxygen release is not reversible in the present study; thus we did not observe the healing of cracks that was reported for lithium-/manganese-rich cathode materials upon electrochemical cycling.[51] In practical applications, oxygen release and thermal runaway can lead to severe phase transformation of active materials, chemical decomposition of the electrolyte, and severe unmanageable safety hazards.

Intragranular cracks were also observed in individual particles after *in situ* heating by using 3D STEM tomography. Figure 4 shows four representative photographs of various viewing directions of the two primary particles. Viewing the particle at different cross sections through the 3D STEM tomography showed that a large number of pores were present at the outer surface of the particles (Figure 4 and Movie S2). However, there are two cracks of around 80 nm that are only noticeable when observing the inside of the particle from specific orientations or cross sections, which indicates that the cracks terminate in the particle (Movie S2 and Figure 4b−d). Furthermore, the small particle (Figure 4d) exfoliated due to the short element migration distance compared to the adjacent large particle, which is the direct consequence of oxygen release and structural collapse. Intragranular cracks are mainly formed due to the development, transformation, and propagation of defects, vacancies, and dislocations. More extensive and irreversible crack formation is observed by transmission synchrotron X-ray tomography for commercial NMC materials after a long period of electrochemical cycling (Figure S5). The


DOI: 10.1021/acs.nanolett.8b01036
Nano Lett. XXXX, XXX, XXX−XXX

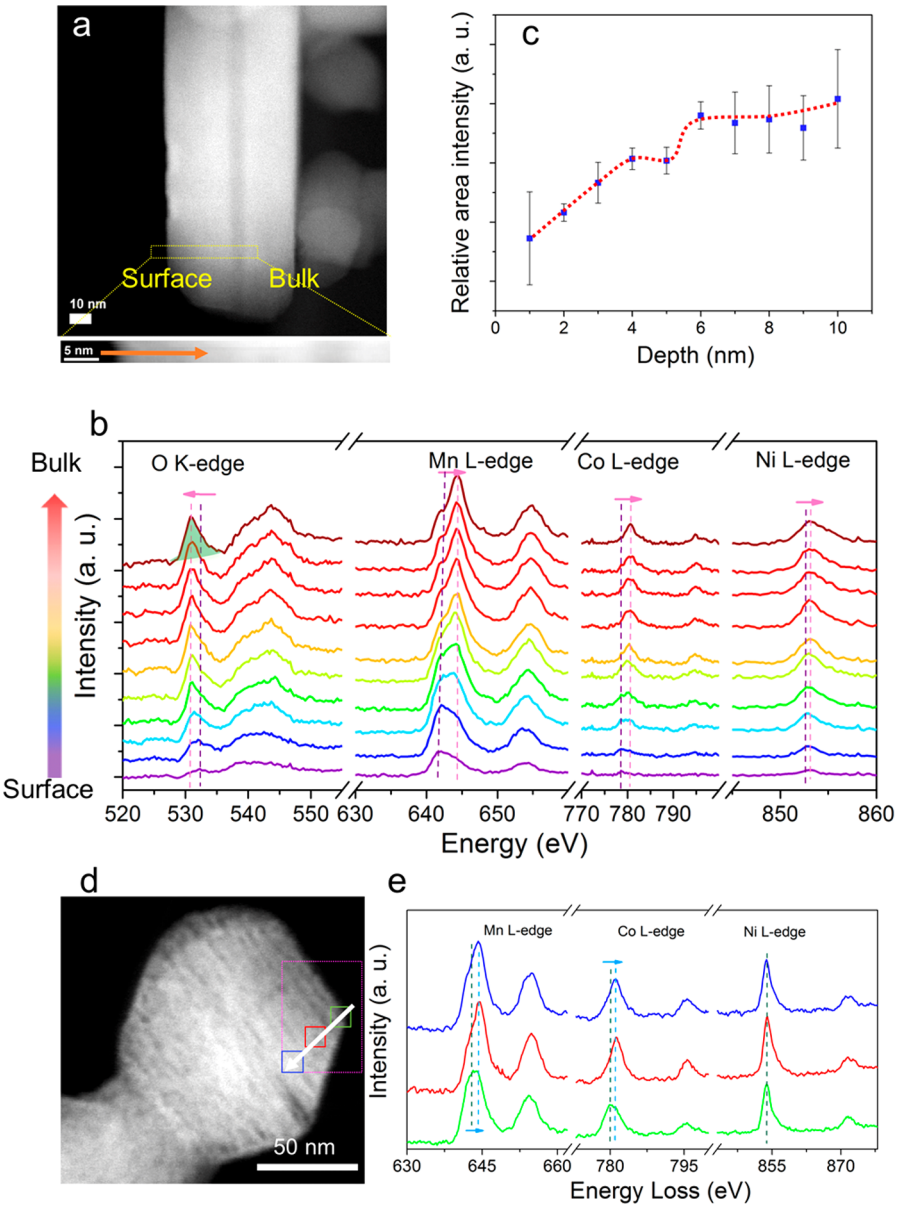


**Figure 3.** STEM-EELS analysis of NMC particles before (a–c) and after (d–e) thermal treatment. (a) STEM image shows the selected region on a delithiated NMC particle, where EELS spectra were collected. (b) EELS spectra of O K-edge, Mn L-edge, Co L-edge, and Ni L-edge corresponding to the selected region in part a. The line scanning direction from surface to bulk had a step size of 1 nm. (c) Normalized integrated intensity of the TM 3d–O 2p hybridization states, with the integrated intensity in a positive relationship with the hole concentration in the $TMO_6$ octahedral cluster. The error bars were created based on standard deviations of spectra collected at equivalent depths in three different regions of the same particle. The dashed line is added to guide the visualization. (d) STEM image shows the selected region on a thermally treated NMC particle, where EELS spectra were collected. (e) EELS spectra of Mn L-edge, Co L-edge, and Ni L-edge corresponding to the selected region in part d with identical color schemes. The energy shift of the $L_3$-edge is indicated by dashed lines and arrows. The EELS spectra were calibrated based on the energy of $Mn^{2+}$ L-edge.

chemical delithiation can induce crack formation due to the fact that the concentrated oxidant used to rapidly oxidize the host structure can result in stress buildup and cracks. This process occurs too rapidly to be studied by *in situ* ETEM. The crack formation during prolonged electrochemical delithiation/lithiation has been well reported by the literature, but the cracks usually accumulate after a large number of cycles (Figure S5) thus inhibiting the *in situ* ETEM study. To facilitate the *in situ* observation, we took advantage of oxygen release of charged NMC particles under thermally activated conditions to mimic the oxygen release and crack formation under prolonged battery cycling. For this study, we carefully chose clusters of primary particles that were free of cracks caused by the chemical delithiation. Combining with our and other researchers' earlier finding that extensive oxygen loss and metal reduction occurred at the surface of NMC particles after long-term cycling at room temperature,[4,31,36,52] the X-ray tomography results are consistent with the *in situ* heating observation, which validates the applicability of our finding to conventional cycling conditions.

Considering that the continuous electron beam radiation could potentially damage the structure[53,54] and affect the intergranular crack and pore formation, *ex situ* heating experiments were conducted. The delithiated NMC powders


DOI: 10.1021/acs.nanolett.8b01036
*Nano Lett.* XXXX, XXX, XXX–XXX

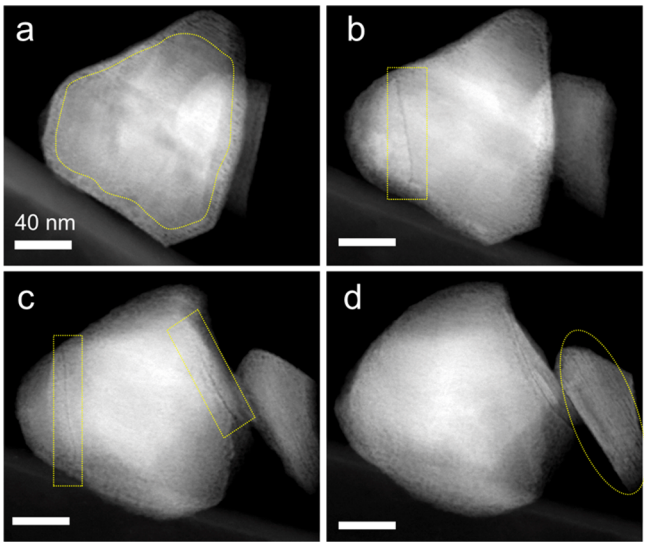


**Figure 4.** (a–d) STEM images for the same two particles taken from different directions to exhibit the 3D view of delithiated NMC particles after *in situ* heating on a TEM grid. The regions enclosed by yellow dashed curves display intragranular cracks. The scale bars are 40 nm for all images.

were placed in an environmental chamber and kept at 230 °C for 3 h. EELS and TEM images of the *ex situ* sample were taken to compare with the *in situ* heating sample. Note that the intergranular cracks, surface pores, and layer exfoliation were all present in the same image (Figure S6). Meanwhile, there were no major differences between the TM L-edge EELS spectra of the *in situ* heated sample and the *ex situ* heated powder (Figure S7), which means that the valence change, structural transformation, and formation of cracks are attributable to the abusive thermal conditions and not to the long-term electron beam irradiation. The present study indicates that if methods (*e.g.*, doping, coating) can be developed to sufficiently inhibit oxygen loss upon electrochemical cycling, the chemomechanical properties of NMC materials will be improved, particularly for nickel-rich NMC materials.

The chemomechanical failure of NMC particles was theoretically studied using finite element method. The surface stress is about two orders magnitudes smaller than the bulk stress. Therefore, in the finite element modeling, we have ignored the effect of surface tension. Previous studies reported that the layered-to-spinel phase transition was accompanied by an anisotropic volumetric strain (the ratio of the lattice constants $c_{hex}/a_{hex}$ = 5.07 in the layered structure decreased to 4.89 in the spinel and rocksalt phases).[55] Consequently, NMC particles aggregated with different grain orientations (Figure f5

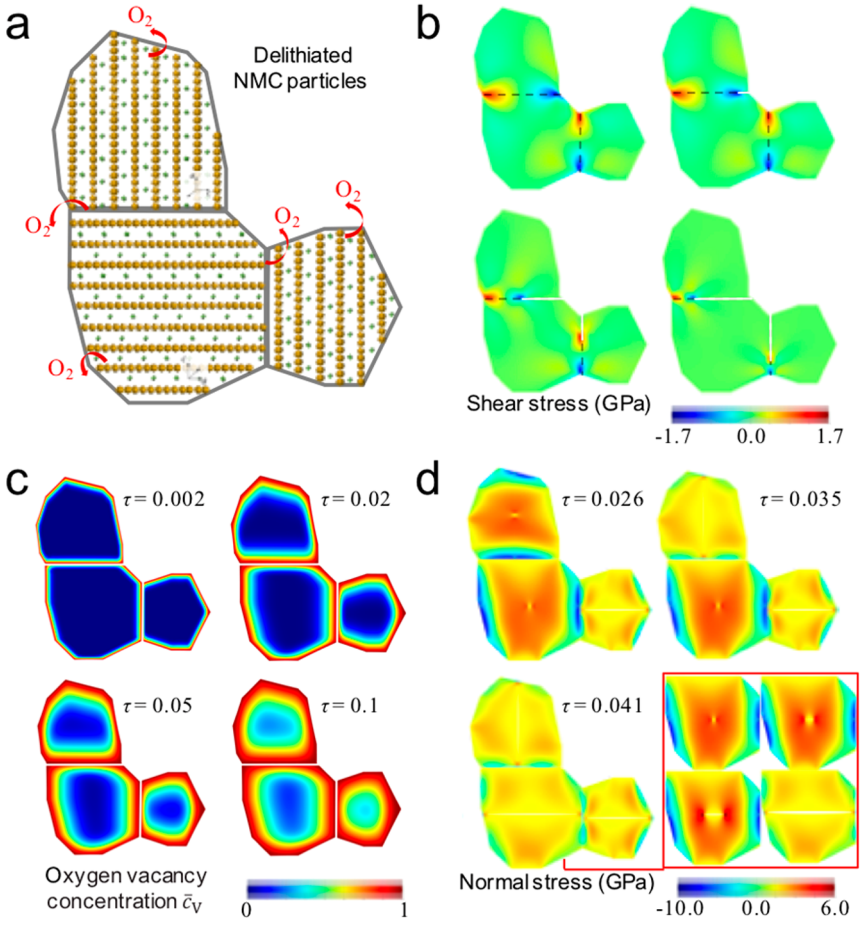


**Figure 5.** (a) Finite element modeling (FEM) model consisting of multiple NMC grains of different orientations. (b) Evolution of shear stress along the grain boundaries and associated intergranular cracks induced by the phase transformation of NMC. (c) Profile of the oxygen vacancies, and (d) nucleation and propagation of intragranular cracks induced by oxygen release in NMC. The inset in part d shows the initiation and rapid propagation of the intragranular crack in the lower left NMC grain.



DOI: 10.1021/acs.nanolett.8b01036
*Nano Lett.* XXXX, XXX, XXX–XXX

5a) are subject to mismatch strains at the grain boundaries and shear stresses. The stress field facilitates intergranular cracks to initiate at the grain edges and rapidly propagate along the grain boundaries. Figure 5b shows the snapshots of the intergranular cracks. The shear stress is partially released after the channel cracks propagate through the grain boundaries.

Figure 5c depicts the distribution of oxygen vacancy concentration within the NMC grains as a function of the normalized time $\tau = D_O t/L^2$, where $L$ represents the characteristic size of the NMC grain. The characteristic time scale for oxygen transport is much longer than that of phase transition. In addition, the chemical stability of the layered structure before the phase transition prohibits the oxygen release,[55] while the fresh surface created by the phase transition induced cracks largely accelerates oxygen release. We believe that oxygen loss mostly accompanies the phase transition. Here we model the strains and cracks induced by the phase transition and oxygen release separately. The oxygen vacancies within NMC grains are inhomogeneously distributed because of the orientation-dependent oxygen release rate.[56] Figure 5c shows the evolution of the oxygen vacancies over time. The formation of oxygen vacancies triggers considerable lattice expansion in NMC.[57] The gradient of oxygen vacancy induces a field of mismatch strain and thus stresses along the NMC grains as well as within the grains, appending the shear stresses along the grain boundaries caused by the phase transition. The resulting stress field promotes intergranular cracks. Upon oxygen release, the outer shell, which is enriched in oxygen vacancies, undergoes a larger expansion than the core regime, generating a compressive stress field near the surface and tensile stresses at the center (Figure 5d). As a consequence, the tensile stresses at the center of a grain initiate and propagate an unstable radial crack and cause breakdown of NMC grains, which are shown in the inset of Figure 5d. The nucleation and propagation direction of intragranular cracks depend on the profile of the oxygen vacancies, the geometry of NMC grains, as well as the size and orientation of the pre-existing defects. Therefore, one can safely conclude that the FEM analysis is consistent with our experimental observation, and the integrative approach of experiments and modeling offer a good path toward understanding the chemomechanical properties of cathode materials.

In conclusion, thermal and chemomechanical stability are important for evaluating lithium ion batteries in terms of their cycle life and safety characteristics. The oxygen activity and evolution in NMC cathode materials, especially when charged to high voltages and under thermal abuse conditions, can create chemical and structural transformations that directly impact the chemomechanical stability. By virtue of *in situ* ETEM and synchrotron X-ray spectroscopy, we studied the oxygen release induced chemomechanical breakdown of charged NMC materials. Specifically, we observed the formation of inter- and intragranular cracks, pores, and layer−layer exfoliation during the events of oxygen release, transition metal reduction, and structural transformation. Additionally, the growth process of intergranular cracks was quantified and monitored through the finite element modeling, which indicated that the oxygen release triggered the chemomechanical breakdown of delithiated NMC materials. The crack incubation probed by *in situ* ETEM and modeled by FEM analysis suggests that the oxygen release induced phase transformation needs to be accumulated to a certain degree before a crack can be initiated. This could potentially explain the less severe crack formation when NMC materials are cycled at lower voltages.[26] Although practical batteries are operated at lower temperatures than the *in situ* heating study, our results reveal the interrelationship between orbital occupancy, and thermal and chemomechanical stability, and provide a chemical basis for future studies of the oxygen activity and safety characteristics in oxide cathode materials. The further improvement of these materials should focus on not only using conventional doping, substitution, and coating methods to stabilize against oxygen release, but also effectively minimizing the mechanical consequence of oxygen release under various scenarios of battery usage, such as high voltages and/or high temperature.

**Experimental Section.** *Synthesis Method.* $LiNi_{0.4}Mn_{0.4}Co_{0.2}O_2$ was synthesized using a coprecipitation method with $NiSO_4{\cdot}6H_2O$ (Sigma-Aldrich, 99.99%), $MnSO_4{\cdot}H_2O$ (Sigma-Aldrich, 99%), and $CoSO_4{\cdot}7H_2O$ (Sigma-Aldrich, 99%) as the raw materials. The transition metal solution (0.04 M $NiSO_4{\cdot}6H_2O$, 0.04 M $MnSO_4{\cdot}H_2O$, and 0.02 M $CoSO_4{\cdot}7H_2O$ dissolved in 100 mL of $H_2O$), starting solution (40 mL of NaOH and $NH_3{\cdot}H_2O$ aqueous solution with a molar ratio $NaOH/NH_3$ = 1.2, pH value was adjusted to 10.5), and base solution (100 mL of NaOH and $NH_3{\cdot}H_2O$ aqueous solution with a molar ratio $NaOH/NH_3$ = 1.2) were made and separately stored in Kimble bottles. The transition metal solution and base solution were simultaneously pumped into the starting solution at a drop rate of ∼2 mL/min with continuous stirring at 50 °C under the $N_2$ protection. The drop rate of the base solution was frequently tuned to keep the pH at 10.5 ± 0.2. The precipitate was collected, washed, and filtrated with deionized (DI) water and dried in vacuum oven overnight at 100 °C. The dried precursor was then mixed with LiOH thoroughly and calcined under air flow (2 L/min) at 725 °C for 6 h to obtain the final $LiNi_{0.4}Mn_{0.4}Co_{0.2}O_2$ powder. Subsequently, we used $LiNi_{0.4}Mn_{0.4}Co_{0.2}O_2$ to obtain delithiated $Li_{1-x}Ni_{0.4}Mn_{0.4}Co_{0.2}O_2$ particles by chemical delithiation. Briefly, 1 g of $LiNi_{0.4}Mn_{0.4}Co_{0.2}O_2$ powder was dispersed in 0.11 M $NO_2BF_4$ (Acros Organic, 97%) dissolved in acetonitrile ($CH_3CN$, Fisher Chemical, 99.9%), and continuously stirred for 24 h in an Ar-filled glovebox ($H_2O$ < 0.5 ppm, $O_2$ < 0.5 ppm) at room temperature. Then, the delithiated powder was collected and washed three times using acetonitrile. Finally, the $Li_{1-x}Ni_{0.4}Mn_{0.4}Co_{0.2}O_2$ product was dried overnight. The delithiated samples were handled with caution to limit the exposure to the ambient air, which was shown to be sufficient to protect the surface chemistry of delithiated NMCs.[41]

*Materials Characterization.* XRD was performed at beamline 11-3 of SSRL. Transmission XRD ring patterns were detected. $LaB_6$ patterns were collected as reference data for calibration, and exposure time was only 0.5 s for the samples to avoid any saturation. Scanning electron microscopy (SEM) was performed on a JEOL JSM-7000F instrument with a Thermo Scientific EDS (energy dispersive X-ray spectroscopy) detector. Hard X-ray Raman scattering (XRS) measurements were performed at beamline 6-2B at SSRL. The spectra were recorded with samples kept in helium atmosphere, and each spectrum was a bandwidth of 0.55 eV; the incident photon energy was selected with a double-crystal average of multiple spectra collected over the 2 h period. The X-ray Raman signals were collected with Si-660 reflection of the 40-crystal XRS spectrometer at 9694.8 eV with a monochromator Si (311) around 10.3 keV to have the Raman offset corresponding to Mn L2,3-edges, Co L2,3-edges, and Ni L2,3-edges. Soft XAS measurements were performed on the 31-pole wiggler beamline 10-1 at Stanford Synchrotron Radiation Lightsource (SSRL)


DOI: 10.1021/acs.nanolett.8b01036
Nano Lett. XXXX, XXX, XXX−XXX

using a ring current of 350 mA and a 1000 L/mm spherical grating monochromator with 20 $\mu$m entrance and exit slits, providing ~$10^{11}$ ph/s at 0.2 eV resolution in a 1 $mm^2$ beam spot. Data were acquired under ultrahigh vacuum ($10^{-9}$ Torr) in a single load at room temperature using total electron yield (TEY), where the sample drain current was collected, and in the fluorescence yield (FY), where a silicon diode (IRD AXUV-100) was used to collect the FY positioned near the sample surface. All spectra were normalized by the current from freshly evaporated gold on a fine grid positioned upstream of the main chamber. The transmission X-ray tomography was performed at beamline 6-2c at SSRL. An in-house developed software package known as TXM-Wizard was used for the analysis of all the tomography results.

*In Situ Heating.* Delithiated NMC particles were loaded on a silicon nitride passivated silicon chip. The particles were subsequently heated at 235 °C by a local Joule heating element integrated on the silicon chip. All *in situ* S/TEM images and movies were recorded on a FEI Environmental Titan instrument operated at 300 keV. A Denssolution MEMS heating holder (Model Wildfire S3) was used to heat the particles. Helium was flown through the objective volume in the environmental TEM, and a pressure of 0.2 mbar in the sample area was maintained during the *in situ* heating experiment. *Ex situ* TEM images and electron energy loss spectra (EELS) were acquired on a JEOL 2100 S/TEM instrument operated at 200 keV.

*Methodology of Finite Element Modeling.* We performed finite element simulations (FEM) to understand the stress and intergranular/intragranular cracks in NMC under thermal abuse conditions. Delithiated NMC is subject to the strain field, $\varepsilon = \varepsilon_{TE} + \varepsilon_{PT} + \varepsilon_{OR}$, where $\varepsilon_{TE}$, $\varepsilon_{PT}$, and $\varepsilon_{OR}$ represent the strains induced by thermal expansion, phase transition, and oxygen release, respectively. $\varepsilon_{TE}$ is considerably smaller than the strains induced by phase transition and oxygen release.[55,57] Here we have ignored $\varepsilon_{TE}$ in the modeling. The phase-transition strain $\varepsilon_{PT}$ is highly anisotropic. A prior study using *in situ* XRD measurements determined that the lattice constants along *a* and *c* directions increased by 4.48% and 0.74% upon the phase transition from the layered to spinel-like/rocksalt structures, resulting in a triaxial strain field: $\varepsilon_a = \varepsilon_b = 4.48\%$ and $\varepsilon_c = 0.74\%$.[55] For the oxygen release induced strain $\varepsilon_{OR}$, it is assumed to be proportional to the normalized oxygen vacancy concentration $\bar{c}_V$, $\varepsilon_{OR} = 1/3\beta_c\bar{c}_V$, where $\beta_c$ represents the chemical expansivity dictating the volumetric change caused by the formation of oxygen vacancy.[57] $\bar{c}_V$ is related with the normalized oxygen concentration $\bar{c}_O$, $\bar{c}_V = 1 - \bar{c}_O$, where $\bar{c}_O$ is defined as the ratio of the oxygen concentration $c_O$ upon oxygen release to the initial value $(c_O)_{in}$, $\bar{c}_O = c_O/(c_O)_{in}$. The kinetics of oxygen release is assumed to follow Fick's law, $dc_O/dt = D_O\nabla^2 c_O$, where $D_O$ is the diffusivity of oxygen in NMC. Similar to Li diffusion in the layered structure, oxygen diffusion is dependent on orientation where the release rate within the $a-b$ plane is faster than that along the *c* direction.[4] The strain fields $\varepsilon_{PT}$ and $\varepsilon_{OR}$ serve as the input of the FEM model, and the stress field is solved within the framework of elasticity theory. The cohesive zone model is employed to simulate the nucleation and propagation of intergranular/intragranular cracks.[38] When the energy release rate reaches the fracture toughness of the grain boundaries or the interior grains, intergranular or intragranular cracks initiate and propagate. All the parameters used in simulation are listed in Table S1.

## ■ ASSOCIATED CONTENT

### Supporting Information

The Supporting Information is available free of charge on the ACS Publications website at DOI: 10.1021/acs.nanolett.8b01036.

Additional data and figures including STEM images, TEM images, soft XAS spectra, transition X-ray tomography, and large-area EELS (PDF)

Movie S1: representative accelerated STEM results (MPG)

Movie S2: particle at different cross sections through the 3D STEM tomography (MPG)

## ■ AUTHOR INFORMATION


### Corresponding Authors

*E-mail: hxin@bnl.gov.

*E-mail: fenglin@vt.edu.

### ORCID

Marca M. Doeff: 0000-0002-2148-8047

Yijin Liu: 0000-0002-8417-2488

Kejie Zhao: 0000-0001-5030-7412

Feng Lin: 0000-0002-3729-3148


### Author Contributions

L.M., M.M.D., H.L.X., and F.L. participated in conceiving and designing the project. L.M., R.L., L.H., S.X., D.S., J.D.S., T.C.W., D.N., Y.L., H.L.X., and F.L. all participated in performing experiments. R.X. and K.Z. performed and wrote finite element modeling. L.M. and F.L. wrote the manuscript with help from all coauthors. F.L. directed the project.

### Notes

The authors declare no competing financial interest.

## ■ ACKNOWLEDGMENTS


The work at Virginia Tech was supported by Virginia Tech Department of Chemistry startup funds and Ralph E. Powe Junior Faculty Enhancement Award. The work at LBNL was supported by the Assistant Secretary for Energy Efficiency and Renewable Energy, Office of Vehicle Technologies of the U.S. Department of Energy under Contract DE-AC02-05CH11231. The Stanford Synchrotron Radiation Lightsource, a Directorate of SLAC National Accelerator Laboratory and an Office of Science User Facility, is operated for the US Department of Energy Office of Science by Stanford University. Use of the Stanford Synchrotron Radiation Lightsource, SLAC National Accelerator Laboratory, is supported by the US Department of Energy, Office of Science, Office of Basic Energy Sciences under Contract DE-AC02-76SF00515. The work at BNL was supported by the Center for Functional Nanomaterials, which is a U.S. DOE Office of Science Facility, at Brookhaven National Laboratory under Contract DE-SC0012704.


## ■ REFERENCES


(1) Armand, M.; Tarascon, J. M. *Nature* **2008**, *451*, 652.

(2) Liu, W.; Oh, P.; Liu, X.; Lee, M. J.; Cho, W.; Chae, S.; Kim, Y.; Cho, J. *Angew. Chem., Int. Ed.* **2015**, *54* (15), 4440−57.

(3) Xu, J.; Lin, F.; Doeff, M. M.; Tong, W. *J. Mater. Chem. A* **2017**, *5* (3), 874−901.

(4) Lin, F.; Markus, I. M.; Nordlund, D.; Weng, T. C.; Asta, M. D.; Xin, H. L.; Doeff, M. M. *Nat. Commun.* **2014**, *5*, 3529.

(5) Jung, S.-K.; Gwon, H.; Hong, J.; Park, K.-Y.; Seo, D.-H.; Kim, H.; Hyun, J.; Yang, W.; Kang, K. *Adv. Energy Mater.* **2014**, *4* (1), 1300787.




DOI: 10.1021/acs.nanolett.8b01036
*Nano Lett.* XXXX, XXX, XXX−XXX

(6) Liu, G.; Zheng, H.; Simens, A. S.; Minor, A. M.; Song, X.; Battaglia, V. S. *J. Electrochem. Soc.* **2007**, *154* (12), A1129−A1134.
(7) Zheng, H.; Li, J.; Song, X.; Liu, G.; Battaglia, V. S. *Electrochim. Acta* **2012**, *71*, 258−265.
(8) Vasconcelos, L. S. d.; Xu, R.; Li, J.; Zhao, K. *Extreme Mech Lett.* **2016**, *9*, 495−502.
(9) Zhao, K.; Pharr, M.; Vlassak, J. J.; Suo, Z. *J. Appl. Phys.* **2010**, *108* (7), 073517.
(10) Finegan, D. P.; Scheel, M.; Robinson, J. B.; Tjaden, B.; Hunt, I.; Mason, T. J.; Millichamp, J.; Di Michiel, M.; Offer, G. J.; Hinds, G.; Brett, D. J. L.; Shearing, P. R. *Nat. Commun.* **2015**, *6*, 6924.
(11) Xiong, D. J.; Ellis, L. D.; Nelson, K. J.; Hynes, T.; Petibon, R.; Dahn, J. R. *J. Electrochem. Soc.* **2016**, *163* (14), A3069−A3077.
(12) Arumugam, R. S.; Ma, L.; Li, J.; Xia, X.; Paulsen, J. M.; Dahn, J. R. *J. Electrochem. Soc.* **2016**, *163* (13), A2531−A2538.
(13) Wu, Z.; Han, X.; Zheng, J.; Wei, Y.; Qiao, R.; Shen, F.; Dai, J.; Hu, L.; Xu, K.; Lin, Y.; Yang, W.; Pan, F. *Nano Lett.* **2014**, *14* (8), 4700−4706.
(14) Lee, M. H.; Kang, Y. J.; Myung, S. T.; Sun, Y. K. *Electrochim. Acta* **2004**, *50* (4), 939−948.
(15) Sun, Y.-K.; Chen, Z.; Noh, H.-J.; Lee, D.-J.; Jung, H.-G.; Ren, Y.; Wang, S.; Yoon, C. S.; Myung, S.-T.; Amine, K. *Nat. Mater.* **2012**, *11* (11), 942−947.
(16) Kim, M. G.; Cho, J. *Adv. Funct. Mater.* **2009**, *19* (10), 1497−1514.
(17) Lim, J. M.; Hwang, T.; Kim, D.; Park, M. S.; Cho, K.; Cho, M. *Sci. Rep.* **2017**, *7*, 39669.
(18) Xu, K. *Chem. Rev.* **2004**, *104* (10), 4303−4418.
(19) Xu, K. *Chem. Rev.* **2014**, *114* (23), 11503−11618.
(20) Zheng, H.; Sun, Q.; Liu, G.; Song, X.; Battaglia, V. S. *J. Power Sources* **2012**, *207*, 134−140.
(21) Luo, K.; Roberts, M. R.; Hao, R.; Guerrini, N.; Pickup, D. M.; Liu, Y. S.; Edstrom, K.; Guo, J.; Chadwick, A. V.; Duda, L. C.; Bruce, P. G. *Nat. Chem.* **2016**, *8* (7), 684−91.
(22) Seo, D. H.; Lee, J.; Urban, A.; Malik, R.; Kang, S.; Ceder, G. *Nat. Chem.* **2016**, *8* (7), 692−7.
(23) Sathiya, M.; Rousse, G.; Ramesha, K.; Laisa, C. P.; Vezin, H.; Sougrati, M. T.; Doublet, M. L.; Foix, D.; Gonbeau, D.; Walker, W.; Prakash, A. S.; Ben Hassine, M.; Dupont, L.; Tarascon, J. M. *Nat. Mater.* **2013**, *12* (9), 827−35.
(24) Lin, F.; Nordlund, D.; Markus, I. M.; Weng, T.-C.; Xin, H. L.; Doeff, M. M. *Energy Environ. Sci.* **2014**, *7* (9), 3077−3085.
(25) Xu, B.; Fell, C. R.; Chi, M.; Meng, Y. S. *Energy Environ. Sci.* **2011**, *4* (6), 2223−2233.
(26) Yan, P.; Zheng, J.; Gu, M.; Xiao, J.; Zhang, J. G.; Wang, C. M. *Nat. Commun.* **2017**, *8*, 14101.
(27) Ryu, H.-H.; Park, K.-J.; Yoon, C. S.; Sun, Y.-K. *Chem. Mater.* **2018**, *30* (3), 1155−1163.
(28) Shen, C. H.; Wang, Q.; Chen, H. J.; Shi, C. G.; Zhang, H. Y.; Huang, L.; Li, J. T.; Sun, S. G. *ACS Appl. Mater. Interfaces* **2016**, *8* (51), 35323−35335.
(29) Zheng, J.; Gu, M.; Xiao, J.; Zuo, P.; Wang, C.; Zhang, J.-G. *Nano Lett.* **2013**, *13* (8), 3824−3830.
(30) Mukhopadhyay, A.; Sheldon, B. W. *Prog. Mater. Sci.* **2014**, *63*, 58−116.
(31) Wu, L.; Nam, K.-W.; Wang, X.; Zhou, Y.; Zheng, J.-C.; Yang, X.-Q.; Zhu, Y. *Chem. Mater.* **2011**, *23* (17), 3953−3960.
(32) Gabrisch, H.; Wilcox, J.; Doeff, M. M. *Electrochem. Solid-State Lett.* **2008**, *11* (3), A25−A29.
(33) Zhao, H.; Qiu, B.; Guo, H.; Jia, K.; Liu, Z.; Xia, Y. *Green Energy & Environment* **2017**, *2* (3), 174−185.
(34) Petersburg, C. F.; Li, Z.; Chernova, N. A.; Whittingham, M. S.; Alamgir, F. M. *J. Mater. Chem.* **2012**, *22* (37), 19993−20000.
(35) Tian, C.; N, D.; Xin, H.; Xu, Y.; Liu, Y.; Sokara, D.; Lin, F.; Doeff, M. *J. Electrochem. Soc.* **2018**, *165* (3), A696−A704.
(36) Abraham, D. P.; Twesten, R. D.; Balasubramanian, M.; Petrov, I.; McBreen, J.; Amine, K. *Electrochem. Commun.* **2002**, *4* (8), 620−625.
(37) Hu, E.; Bak, S.-M.; Liu, J.; Yu, X.; Zhou, Y.; Ehrlich, S. N.; Yang, X.-Q.; Nam, K.-W. *Chem. Mater.* **2014**, *26* (2), 1108−1118.
(38) Xu, R.; de Vasconcelos, L. S.; Shi, J.; Li, J.; Zhao, K. *Exp. Mech.* **2018**, *58*, 549.
(39) Huang, Q.; Li, H.; Gratzel, M.; Wang, Q. *Phys. Chem. Chem. Phys.* **2013**, *15* (6), 1793−1797.
(40) Colligan, N.; Augustyn, V.; Manthiram, A. *J. Phys. Chem. C* **2015**, *119* (5), 2335−2340.
(41) Tian, C.; Xu, Y.; Nordlund, D.; Lin, F.; Liu, J.; Sun, Z.; Liu, Y.; Doeff, M. *Joule* **2018**, *2*, 464−477.
(42) Kuiper, P.; Kruizinga, G.; Ghijsen, J.; Sawatzky, G. A.; Verweij, H. *Phys. Rev. Lett.* **1989**, *62* (2), 221−224.
(43) Ma, C.; Alvarado, J.; Xu, J.; Clement, R. J.; Kodur, M.; Tong, W.; Grey, C. P.; Meng, Y. S. *J. Am. Chem. Soc.* **2017**, *139* (13), 4835−4845.
(44) Yoon, W.-S.; Balasubramanian, M.; Chung, K. Y.; Yang, X.-Q.; McBreen, J.; Grey, C. P.; Fischer, D. A. *J. Am. Chem. Soc.* **2005**, *127* (49), 17479−17487.
(45) Lin, F.; Nordlund, D.; Pan, T.; Markus, I. M.; Weng, T.-C.; Xin, H. L.; Doeff, M. M. *J. Mater. Chem. A* **2014**, *2* (46), 19833−19840.
(46) Liu, X.; Wang, D.; Liu, G.; Srinivasan, V.; Liu, Z.; Hussain, Z.; Yang, W. *Nat. Commun.* **2013**, *4*, 2568.
(47) Gauthier, M.; Carney, T. J.; Grimaud, A.; Giordano, L.; Pour, N.; Chang, H.-H.; Fenning, D. P.; Lux, S. F.; Paschos, O.; Bauer, C.; Maglia, F.; Lupart, S.; Lamp, P.; Shao-Horn, Y. *J. Phys. Chem. Lett.* **2015**, *6* (22), 4653−4672.
(48) Qiu, B.; Zhang, M.; Wu, L.; Wang, J.; Xia, Y.; Qian, D.; Liu, H.; Hy, S.; Chen, Y.; An, K.; Zhu, Y.; Liu, Z.; Meng, Y. S. *Nat. Commun.* **2016**, *7*, 12108.
(49) Gu, M.; Genc, A.; Belharouak, I.; Wang, D.; Amine, K.; Thevuthasan, S.; Baer, D. R.; Zhang, J.-G.; Browning, N. D.; Liu, J.; Wang, C. *Chem. Mater.* **2013**, *25* (11), 2319−2326.
(50) Zheng, J.; Xu, P.; Gu, M.; Xiao, J.; Browning, N. D.; Yan, P.; Wang, C.; Zhang, J.-G. *Chem. Mater.* **2015**, *27* (4), 1381−1390.
(51) Chen, C. J.; Pang, W. K.; Mori, T.; Peterson, V. K.; Sharma, N.; Lee, P. H.; Wu, S. H.; Wang, C. C.; Song, Y. F.; Liu, R. S. *J. Am. Chem. Soc.* **2016**, *138* (28), 8824−33.
(52) Lin, F.; Nordlund, D.; Li, Y.; Quan, M. K.; Cheng, L.; Weng, T.-C.; Liu, Y.; Xin, H. L.; Doeff, M. M. *Nat. Energy* **2016**, *1*, 15004.
(53) Lin, F.; Markus, I. M.; Doeff, M. M.; Xin, H. L. *Sci. Rep.* **2015**, *4*, 5694.
(54) Lu, P.; Yan, P.; Romero, E.; Spoerke, E. D.; Zhang, J.-G.; Wang, C.-M. *Chem. Mater.* **2015**, *27* (4), 1375−1380.
(55) Yabuuchi, N.; Kim, Y.-T.; Li, H. H.; Shao-Horn, Y. *Chem. Mater.* **2008**, *20* (15), 4936−4951.
(56) Lin, F.; Nordlund, D.; Weng, T.-C.; Zhu, Y.; Ban, C.; Richards, R. M.; Xin, H. L. *Nat. Commun.* **2014**, *5*, 3358.
(57) Adler, S. B. *J. Am. Ceram. Soc.* **2001**, *84* (9), 2117−2119.



DOI: 10.1021/acs.nanolett.8b01036
*Nano Lett.* XXXX, XXX, XXX−XXX